ERDC/GRL TR-20-1

US Army Corps
of Engineers®
Engineer Research and
Development Center

Coincidence Processing of Photon-Sensitive Mapping Lidar Data

Christian Marchant, Ryan Kirkpatrick, and David Ober

February 2020

Geospatial Research Laboratory

The U.S. Army Engineer Research and Development Center (ERDC) solves the nation's toughest engineering and environmental challenges. ERDC develops innovative solutions in civil and military engineering, geospatial sciences, water resources, and environmental sciences for the Army, the Department of Defense, civilian agencies, and our nation's public good. Find out more at www.erdc.usace.army.mil.

To search for other technical reports published by ERDC, visit the ERDC online library at http://acwc.sdp.sirsi.net/client/default.

ERDC/GRL TR-20-1
February 2020

Coincidence Processing of Photon-Sensitive Mapping Lidar Data

Christian Marchant, Ryan Kirkpatrick, and David Ober

Geospatial Research Laboratory
U.S. Army Engineer Research and Development Center
7701 Telegraph Road
Alexandria, VA 22315

Final report

Prepared for U.S. Army Corps of Engineers
Washington, DC 20314-1000

Under Program Element Number 62784
Project Number 855
Task Number 23

Abstract

Photon-sensitive mapping lidar systems are able to image at greater collection area rates and ranges than linear-mode systems. However, these systems also experience greater noise levels due to shot noise, image blur, and dark current, which must be filtered out before the imagery can be exploited. Described in this report is a synthetic test data set of imagery from a notional airborne Geiger-mode lidar. Also described is the Bridge Sign algorithm, which uses a least-squares technique for noise filtering. The algorithm's performance was validated using synthetic test imagery of both a toy scene and of a realistic scene, which were generated using the parameters of a notional airborne Geiger-mode system. Analysis of the results shows the technique effectively removes noise and preserves fine details with good fidelity.

Contents

Figures and Tables

Figures

Table

Preface

This study was conducted for the Engineer Research and Development Center of the U.S. Army Corps of Engineers under PE 62784, Project 855, Task 23 (GeoICUE), FWI FCBCB5 (High Castle FY19). The technical monitor was Dr. Jean Nelson.

The work was performed by the Geospatial Applications Branch of the Topography Imagery and Geospatial Research Division, U.S. Army Engineer Research and Development Center, Geospatial Research Laboratory (ERDC-GRL). At the time of publication, Mr. Todd Sims was Chief; Ms. Martha Kiene was Chief; and Mr. Ritchie Rodebaugh was the Technical Director for ERDC-GRL. The Deputy Director of ERDC-GRL was Ms. Valerie Carney and the Director was Mr. Gary Blohm.

COL Teresa A. Schlosser was the Commander of ERDC, and Dr. David W. Pittman was the Director.

1 Introduction

1.1 Background

Airborne lidar systems have been mapping the Earth's surface since the pioneering flights by the NASA Wallops Airborne Oceanographic Lidar in the 1970s (Bressel et al. 1977). Lidar is able to capture 3D images of terrain at astonishing rates and levels of detail. Photon-sensitive airborne mapping lidar with a micropulse laser was demonstrated in 2001 (Degnan et al. 2008). The Jigsaw sensor demonstrated an airborne photon-sensitive Geiger-mode avalanche photo-diode (GmAPD) focal plane array (FPA) in 2002 (Marino and Davis 2005), which enabled greater area collection rates and ranges than comparable linear-mode lidars. Other airborne Geiger-mode lidars included the Airborne Ladar Imaging Research Testbed (ALIRT) sensor that flew in 2010 (Knowlton 2011), the High-Altitude LIDAR Operations Experiment (HALOE) sensor (Gray 2011), L3Harris' Intelliearth system in 2015 (Stoker et al. 2016), and MIT Lincoln Laboratory's Airborne Optical Systems Test Bed in 2017 (Clifton et al. 2015). All of these Geiger-mode systems experience significant noise and have employed a coincidence processing step for removing the noise from the imagery. Improvements to coincidence processing can improve the performance envelope of such lidar systems. This work describes a coincidence processing algorithm and the synthetic 3D point clouds that were used for validation.

The two manufacturers of GmAPD for airborne applications are Massachusetts Institute of Technology (MIT) Lincoln Laboratory (Albota et al. 2002) and Ball Aerospace, which licensed the technology from Princeton Lightwave (Itzler et al. 2010) in 2018. GmAPD sensors have greatly increased sensitivity and data collection rates compared to sensors that use linear-mode avalanche photo-diodes (APD). Their advantage is that they support relatively lower link-budgets and greater area collection rates compared to linear-mode APD detectors, but their disadvantages are that they are more sensitive to shot noise and dark current, which must be filtered out of the data before it can be exploited. Additionally, the data filtering process must compensate for the blur caused by the laser pulse width, which the peak-finding electronics would otherwise perform in the case of linear-mode lidars. The high collection rates and resulting large quantity of data make these problems more acute.

Geiger-mode detectors operate in the following manner. The detector circuitry begins in a metastable "off" state. A detection occurs when a photon strikes the detector element and causes an electrical current that triggers the circuit to transition into a stable "on" state that cannot detect additional photons. Most GmAPDs in use in lidar systems today are synchronous, which means the entire FPA must reset before each laser pulse so that all detector elements are sensitive. In order to minimize the loss of sensitivity due to noise events, the FPA is not continuously active, but is turned on at a certain range value called the range gate; prior to where detections are expected. Asynchronous GmAPDs have circuitry to reset individual elements after each detection; however, there is still a non-zero recovery time, during which the element would be insensitive. Such asynchronous GmAPD FPAs are currently commercially available from Ball Aerospace (Kondratko et al. 2019), but to date, all GmAPD lidar systems known to the authors have used the synchronous FPAs. The phenomenon that occurs in GmAPD detectors when an FPA element becomes insensitive to additional photons after an initial detection event is termed blocking loss. This phenomenon partially drives how GmAPD detectors are operated and how lidar systems collect data.

A Geiger-mode system records detection events by the FPA elements and their corresponding time-of-flight during sensor operation. The system also records the orientation of the receiver telescope and the sensor position as logged by the inertial measurement unit (IMU) and global positioning system (GPS) receiver. Data processing electronics combine these to calculate a position value for each photon detection event. A level-1 (L1) data file is a binary file that contains the image frame number, FPA element number, and XYZ coordinate for each detection event. A binary file of level-2 (L2) data contains a set of points with XYZ coordinates that represent a three-dimensional scene by spacing the points along reflective surfaces within the scene. The L2 points may additionally have so-called "intensity" values that represent the relative reflectivity of the surfaces. A level-3 (L3) binary file consists of several files of L2 data that have been aggregated together and registered to a standard coordinate system.

1.2 Objective

The Bridge Sign coincidence processing algorithm creates a human-interpretable L2 point cloud from L1 data. The algorithm is designed to balance several competing image characteristics that are necessary for good-quality output. It needs to remove spurious noise points, but

preserve faint objects. It also needs to resolve fine features and arbitrary surface orientation but also show surfaces as smooth and continuous.

1.3 Approach

The Bridge Sign algorithm aggregates and rasterizes photon detections in a way that preserves all the spatial information that was contained in the L1 data. It then filters the raster, identifies density peaks, and exports them as L2 points. This creates a product that preserves scene detail with minimal spurious clutter and is also intuitively interpreted by human viewers.

2 Coincidence Processing Approach

Coincidence processing relies on the coincident location of several L1 detection points close together to estimate whether a detection event was a noise event or a true reflected signal from a real surface. It is the procedure of converting relatively noisy L1 data into the de-noised and more useable L2 data. Power lines, narrow towers, and whip antennas are examples of objects that can be difficult to distinguish from clusters of noise counts. A coincidence processing algorithm may use a form of local averaging and threshold values to distinguish between noise and real objects.

Image resampling techniques using irregularly spaced point clouds have been demonstrated for representing 2D images (Eldar et al. 1997) and 3D images (Amenta and Bern 1999) in many fields, including computer graphics and medical imaging. Previous approaches to reduce 3D imaging lidar measurements to human-interpretable point clouds have used statistical tests to classify all individual detection events as noise or true reflections, and then aggregating groups of true reflections into L2 points. These approaches have included the Maximum A Posteriori Coincidence Processing (MAPCP) algorithm developed by Johns Hopkins University Applied Physics Laboratory (Stevens et al. 2011) and the Multiple-Peak Spatial Coincidence Processing (MPSCP) algorithm developed by the MIT – Lincoln Laboratory (Vasile et al. 2012). Vasile et al. does describe a comparison of the image quality of the output between MPSCP and MAPCP; however, the lidar community does not currently have any standard test images for lidar or a standardized methodology for evaluating image quality. This has prevented us from making direct comparisons of Bridge Sign's output image quality with other coincidence processing algorithms.

Described below is a new approach for coincidence processing as implemented in the Bridge Sign algorithm and its performance using synthetic L1 data from a notional airborne Geiger-mode lidar sensor is shown. The sensor parameters were selected to be typical for airborne Geiger-mode lidar and can be found in Table 1. This algorithm rasterizes the point cloud imagery and uses a least-squares filter to remove noise rather than a statistical test on a point-by-point basis. The algorithm uses sufficiently-fine sample spacing to ensure that the Nyquist criterion is satisfied and spatial frequency information is preserved. As a result, this algorithm creates output images with good interpretability. The Bridge Sign algorithm implements this approach, which was written as a Python script.

Table 1. Parameters of a notional air-borne Geiger-mode mapping lidar sensor.

Parameter	Value
Altitude	3000 m
Speed	100 m/s
Laser pulse rate	2 kHz
FPA dimensions	32 x 128 pixels
Instantaneous field-of-view	30e-6 rad
Probability of detection	50%
Range gate start	2500 m
Range gate stop	3500 m
Range bin size	5 cm
Range jitter standard deviation	5 cm
Angle jitter standard deviation	10e-6 rad
Dark current rate	1500 photons/sec
Sweep rate	20 sweeps/sec
Sweep azimuth	±35e-3 rad

3 Validation Methodology

Our approach uses a synthetic L1 file to validate a coincidence processing algorithm by comparing the output image with the known original scene. Synthetic data functions as its own truth image for comparison with the output imagery. Although field-collected L1 data would be far more realistic and representative of the way lidar sensors are used, it would require significant additional effort to establish a corresponding ground-truth point cloud to go with it. Additionally, we are not aware of any publicly-released field-collected L1 Geiger-mode imagery.

A simple caricature of an artificial scene describes the workflow, as shown in Figure 1. An L2 file is created that contains a pre-programmed artificial scene, represented by Figure 1(a). Then a synthetic L1 file was generated, symbolized by Figure 1(b), using the parameters of the sensor shown in Table 1. The L1 file was input into the Bridge Sign algorithm, which processed it and generated a processed and de-noised L2 file symbolized by Figure 1(c), which we compared to the original scene. Also generated was a synthetic L1 file by using converted genuine terrestrial imagery of a real scene into a synthetic airborne-collected L1 file. A real scene was imaged with a stationary terrestrial linear-mode lidar and the imagery was used as a basis to back-synthesized L1 file based on the parameters in Table 1. This allowed us to test the Bridge Sign algorithm using synthetic L1 data that contained realistically shaped terrain and vegetation.

Figure 1. The synthetic data generation flow process begins with a synthetic scene (red dots left), which is the basis to generate a synthetic L1 binary file (green dots center), which is converted into a coincidence processed L2 binary file (blue dots right).

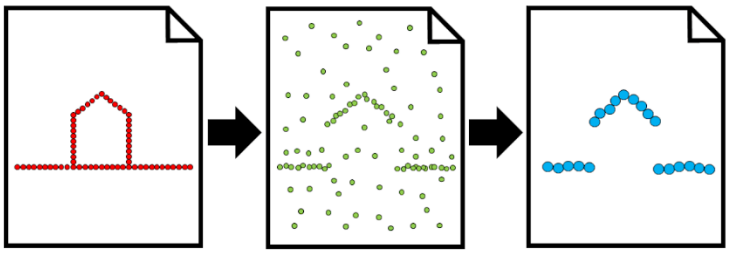

3.1 Artificial scene

A Python script was written to generate an artificial scene, which is shown in Figure 2. The scene is 100 by 100 m and the reflectivity value of the ground surface is 0.5. There is a 10 m diameter circular spoke target with a height of 2 m at the center of the scene with 32 evenly spaces spokes, each with a reflectivity of 1.0, tapering towards the center as illustrated in Figure 3. There is a second identical spoke target covered by a simulated foliage canopy 25 m south of the center. The simulated foliage consists of 49,000 points approximately 5 m above the ground with random uniformly distributed reflectivity and transmissivity values between zero and one. There is another set of simulated foliage 25 m west of the center, but without a spoke target beneath it. North of the scene center are two sets of 36 tri-bar targets, each with a reflectivity of 1.0, positioned two meters above the ground. One set is oriented north-south and the other set is oriented east-west. The relative sizes and orientations of each of the two sets are shown in Figure 4. There is a 2 by 2 by 2 m cube with a reflectivity of 1.0 located 25 m east of the center and a 32 m wide logo painted onto the ground about 40 m south-east of the center. There is a coil-shaped target 35 m south-west of the center. The target is 5 m tall, has two complete loops, a coil diameter of 1.5 m, a tube diameter of .5 m, and a reflectivity of 1.0, as shown in Figure 5.

Figure 2. Artificial scene with test targets.

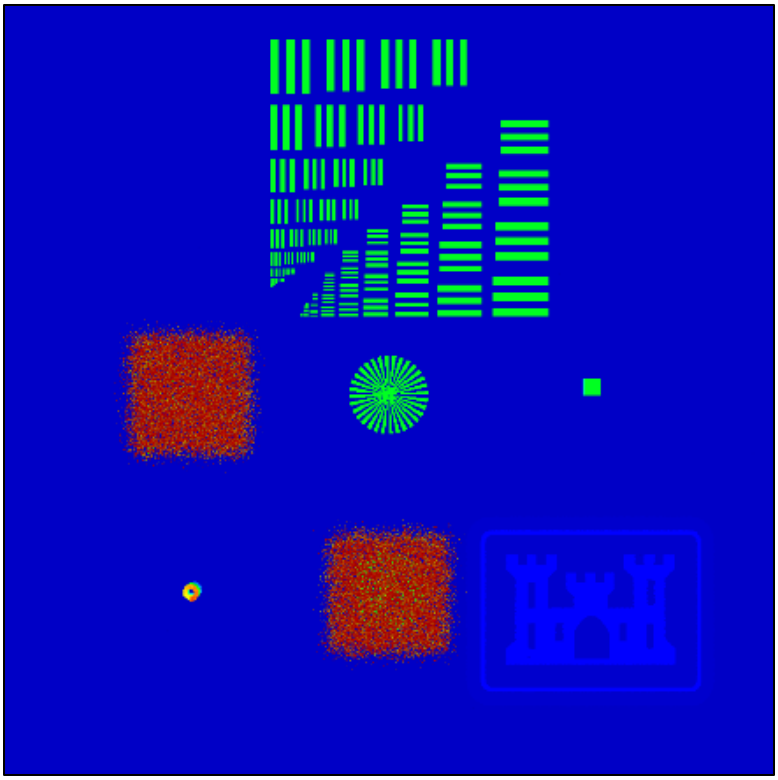

Figure 3. Spoke test target (a) as intended, (b) as synthetic L1 data in the open, (c) after coincidence processing in the open, (d) as synthetic L1 data under foliage, and (e) after coincidence processing under foliage.

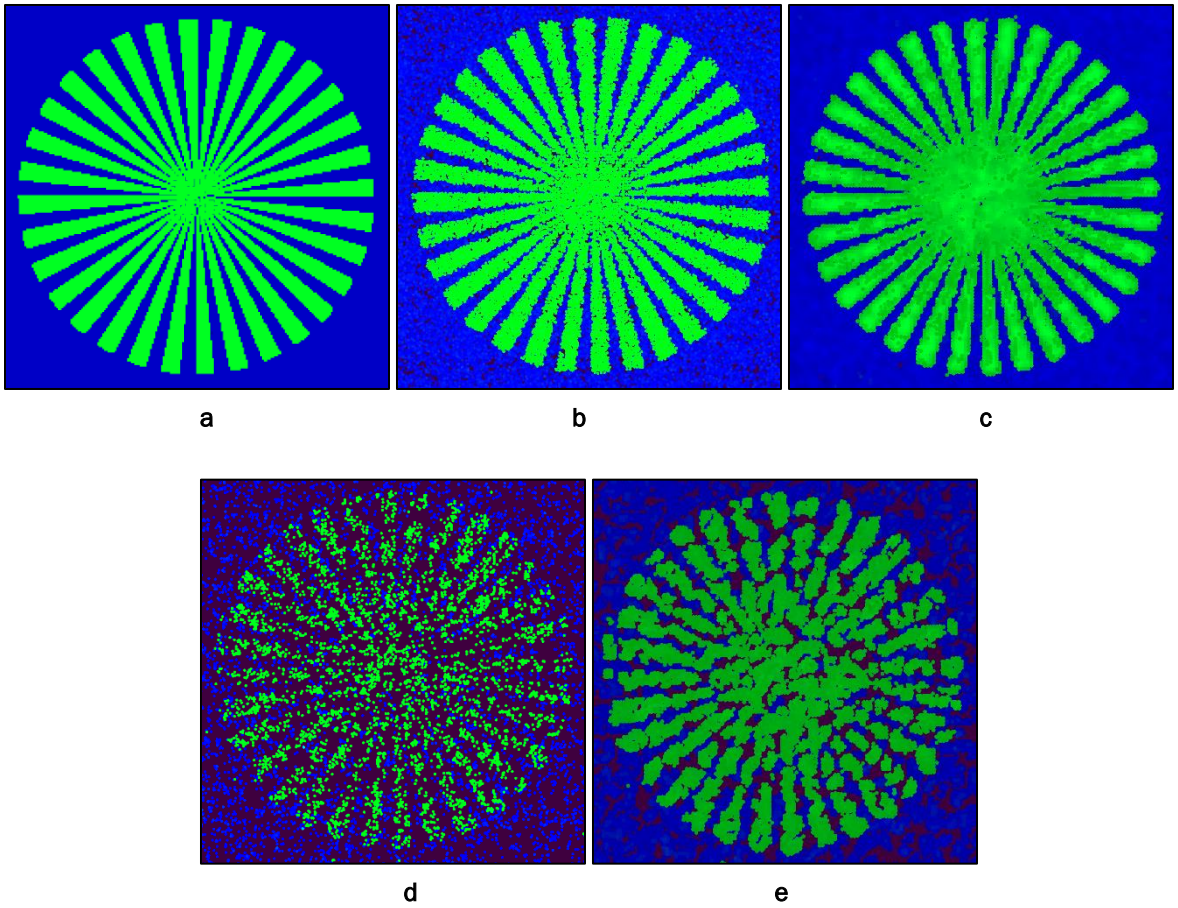

a b c

d e

Figure 4. Tri-bar test targets (a) as intended, (b) as synthetic L1 data, and (c) after coincidence processing.

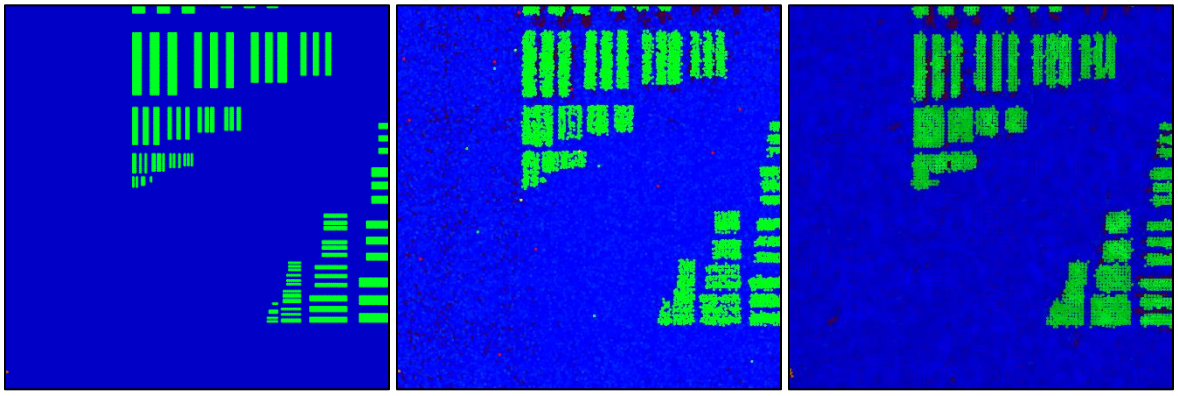

a b c

Figure 5. Coil test target (a) as intended, (b) as synthetic L1 data, (c) and after coincidence processing.

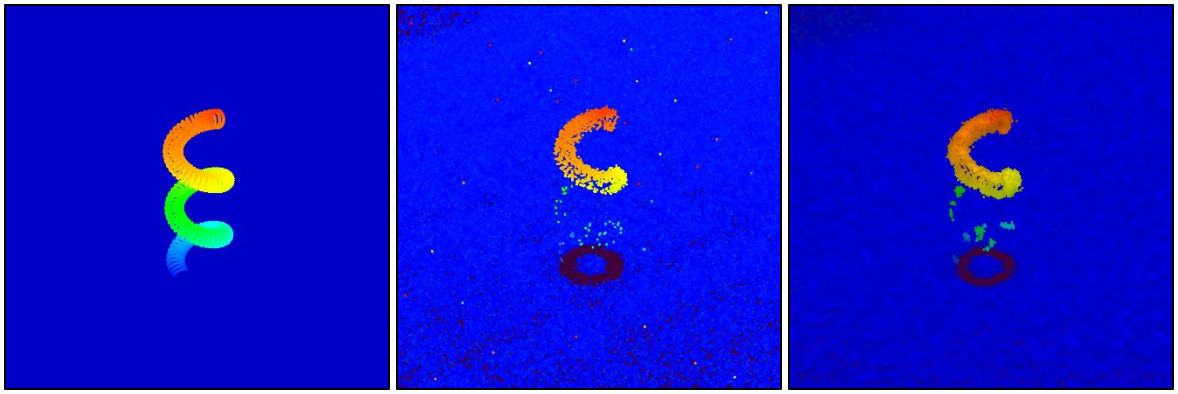

a b c

3.2 Real scene

A set of targets were built on a mowed grass field at the National Geodetic Survey Testing and Training Center near Corbin, Virginia. These were scanned using a stationary terrestrial linear-mode lidar. This allowed us to verify the performance of the algorithm on a scene with realistically shaped terrain and foliage, illustrated in Figure 7(a). The data-synthesis process was applied to the terrestrial lidar data using the same parameters of the notional airborne Geiger-mode sensor. Figure 7(b) shows the corresponding simulated L1 data. The scene contains five sets of horizontal tri-bar targets oriented parallel to the ground and five sets of vertical tri-bar targets oriented perpendicularly to the ground.

3.3 L1 generation process

A process to generate synthetic L1 data was applied to both the artificial and real scenes. A sensor flight path was defined that included four passes over the artificial scene: from south to north, north to south, east to west, and west to east. The sensor's directional view sweeps back and forth through nadir and perpendicular to the flight path at a rate of 20 sweeps per second. The angle swept from nadir is ±35 mrad. The detector camera captures an image frame for each laser pulse.

The L1 data was generated using a rasterization process. The artificial L2 points are originally defined in a world-centric coordinate space, as illustrated by the blue dots in Figure 6(a), using the notional image introduced in Figure 1. The L2 points are projected into the frame-centric coordinate space shown in Figure 6(b) for each image frame, assigning each L2 point to a voxel that corresponds to the row, column, and range

values, for which it was observed by the detector. The reflectivity and transmissivity values of the L2 points are assigned to their corresponding voxels in the frame-centric coordinate space.

Figure 6. Synthetic L2 data points (blue dots) (a) in the world-centric coordinate space and (b) in the frame-centric showing sensor position (yellow dots) and photon detections (red stars).

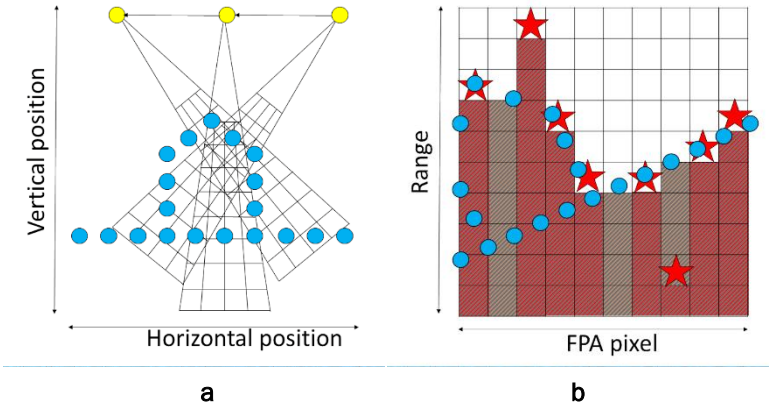

Figure 7. Test range scene with targets (a) as collected by terrestrial tripod-mounted linear-mode lidar, (b) as synthetic L1 data, (c) and after coincidence processing.

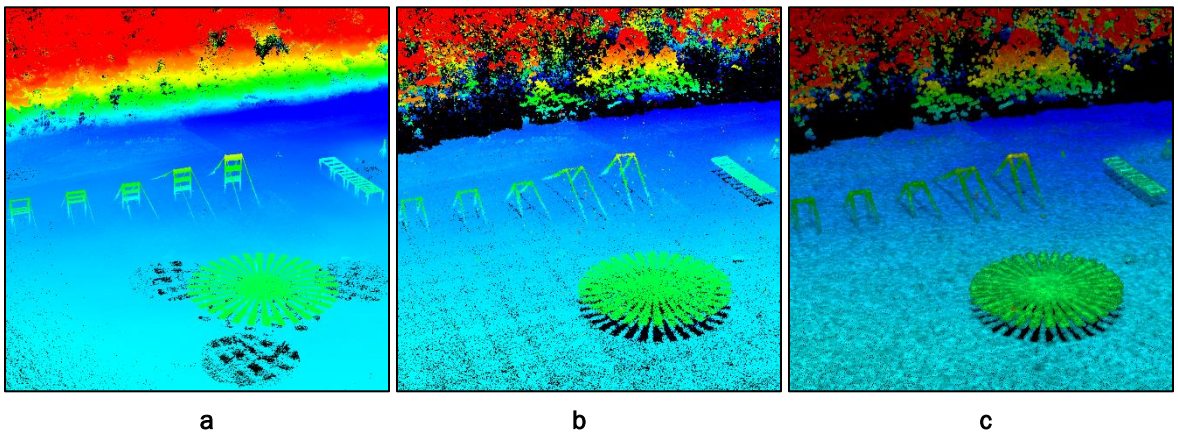

A probability parameter of detecting a photon is computed for each voxel using the reflectivity value that had been previously assigned. For each voxel, all transmissivity values from closer ranges are multiplied together to compute the total transmissivity along the line-of-sight path. The reflectivity value of the voxel is normalized by this total transmissivity value. This normalized reflectivity parameter was used to generate a random number of detected photons with a Poisson distribution. In addition, a noise photon was generated for each FPA element, whose range from the opening of the range gate was modeled as an exponentially distributed random variable. For each FPA element, only the closest range

detection event is retained, shown by the red stars in Figure 6(b), as well as the associated loss of sensitivity due to lidar shadow (gray hatching) and blocking loss (red hatching). This replicates the phenomenon of blocking loss as detailed previously. The XYZ coordinate of each closest detection event is then saved to an L1 file, together with the image frame number and FPA element number.

3.4 Realism of synthetic L1 data

Figures 3(b), 4(b), and 5(b) illustrate the synthetic L1 data. This rasterization approach simulates the image with less fidelity than ray tracing and can generate inaccurate representations of objects. This is because the reflectivity value of a voxel is based on a single L2 point, regardless of whether that L2 point fully subtends the voxel or how many additional L2 points of different reflectivity values are also located within that voxel. For example, if multiple points fall within an array element, then the highest reflectivity value and lowest transmissivity values are used for the entire element. Furthermore, this approach cannot accurately model features that are smaller than the instantaneous field-of-view of a single FPA element, since a single L2 point is modeled as entirely filling the element. This effect is visible in Figure 3(b), where the area at the target center has the same photon density as the wide spoke ends, instead of the 50% density that it should have. Nevertheless, this approach does have sufficient fidelity to model system and algorithm performance and human-perceived image quality. It also has the important advantages of being much easier and faster to implement, debug, and run on the computer.

Figure 3(b) shows the image quality of the exposed spoke target in the L1 point cloud. Inspection of the figure shows that spokes lose definition at approximately 1 m from the target center, which corresponds to a spoke width of 10 cm. Figure 3(d) shows the L1 image quality of the spoke target under foliage. The signal strength decreases due to loss of transmitted power and blocking loss, so spokes cannot be resolved closer than approximately 2 m from the target center, which corresponds to a spoke width of 20 cm.

Figure 4(b) shows details of the 16 smallest tri-bar target sets. The third row from the bottom shows sets bar widths of 15, 12.5, 10, and 9 cm from left to right. The 15 bars are marginally distinguishable and the bars become less distinguishable as they become narrower. The resolution of

the imagery may be limited by the sensor's instantaneous field-of-view (IFOV) value of 30e-6 radians, which corresponds to a minimum ground sample spacing of 9 cm. Figure 5(b) shows a detailed view of the L1 image of the coil target. The notional sensor is downward pointing and sweeping through nadir, which results in strong lidar shadow. This is visible as a black ring of missing returns in the ground surface below the coil target. Furthermore, the top surface of the upper loop is fully visible, but it obscures the lower loop, which only shows sparse returns on the sides.

The synthetic L1 imagery of the real scene demonstrates characteristics of realistic imagery, such as strong lidar shadow due to the nadir collection geometry of the notional sensor and the visibility of only the top surface of the vertical tri-bar targets. Lidar shadow also obscures much of the forest floor below the trees in the scene, although there are patches of ground visible where the sensor achieved successful penetration of gaps in the canopy.

4 Coincidence Processing Steps

The Bridge Sign coincidence processing algorithm converts L1 imagery into L2 point clouds that are suitable for exploitation by human beings. The algorithm first divides the scene into sub-volumes, which it processes independently due to computational resource constraints. The sub-volume dimension is a user-defined parameter, which can be set based on the scale of the lidar data set and the amount of computer memory available to the user. This division of the scene also enables the algorithm to be parallelizable in a future version. The algorithm identifies all FPA image frames, whose line-of-sight intersect each sub-volume and associates them using a data structure. Then, each sub-volume is rasterized into a three-dimensional grid, which is populated by the detections and interrogations from that part of the scene. The raster is de-noised using a least-squares filter and then a surface-finding step identifies local maximum points, which are saved to an L2 output file.

4.1 Rasterization

The flowchart in Figure 8 shows the processing steps of Bridge Sign, which begins by creating a 3D raster of the volume and iterating over every image frame associated with a sub-volume. Each sub-volume of the scene must have sample spacing that is sufficiently fine to capture all information within the signal and also be small enough to fit within computer main memory. The Nyquist sampling theorem requires the sampling rate to be twice the highest frequency within the image in order for a band-limited signal to be completely recovered (Gonzalez and Woods 2008). The original detector signal can be band-limited by the IFOV prior to digitization, the laser pulse width, the diffraction limit of the detector optics, or the bandwidth of the detector circuitry. The algorithm assumes that the maximum spatial frequency is limited by the IFOV and sets the raster voxel size at half its value. As illustrated by Figure 6, the native coordinate space of each image frame is based on the range to the detector and the FPA element index. The detections and interrogations of each image frame are resampled into the world-centric coordinate space using trilinear interpolation. In this way, the algorithm counts the total number of interrogations and detections of photons for each voxel of the raster.

Figure 8. Flow diagram showing the steps and operation of the Bridge Sign algorithm.

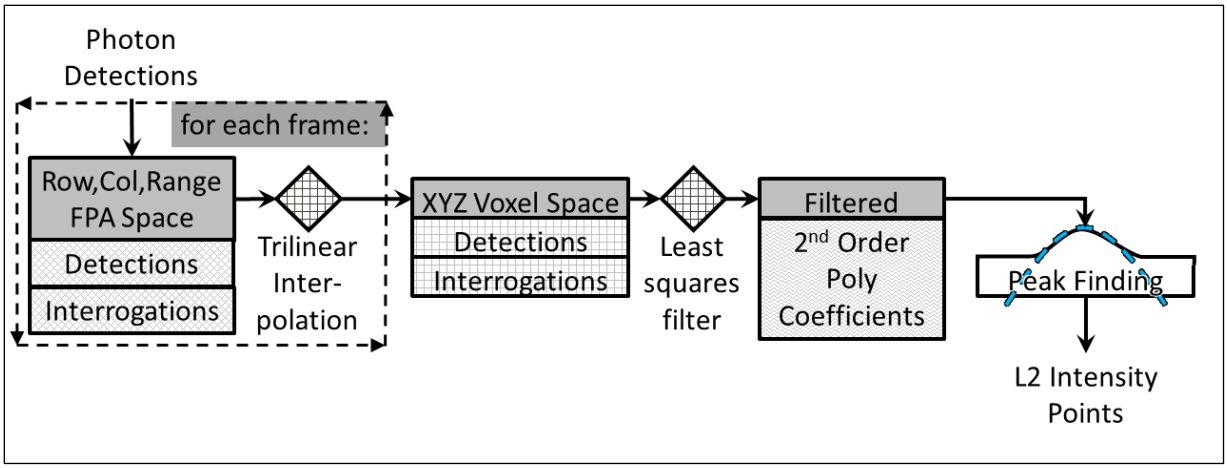

4.2 Least-squares filtering

Once all detections and interrogations have been counted, the algorithm applies a least-squares filter to the raster. The windowed filter iterates over all the voxels in a sub-volume. It centers on each voxel and its neighboring voxels and calculates **c**, the vector of coefficients of a 2nd-order polynomial of a 3D scalar field using least squares. These local polynomials both smooth the image, as shown in Figure 9, and allow the detection of local maxima and saddle points.

The vector $\mathbf{d}_{meas}$ represents the detections of each voxel in a neighborhood, which are shown by Figure 9(a) and the vector $\mathbf{d}_{est}$ represents the polynomial approximation, which is shown by Figure 9(b) and is defined as

$$\mathbf{d}_{est} = M\boldsymbol{c} = |\mathbf{1} \quad \mathbf{x} \quad \mathbf{y} \quad \mathbf{z} \quad \mathbf{x^2} \quad \mathbf{y^2} \quad \mathbf{z^2} \quad \mathbf{xy} \quad \mathbf{xz} \quad \mathbf{yz}| \begin{vmatrix} c_0 \\ c_1 \\ \vdots \\ c_9 \end{vmatrix}, \qquad (1)$$

$$\boldsymbol{c} = (M^T M)^{-1} M^T \boldsymbol{d}_{meas}$$

where **x**, **y**, and **z** are vertical vectors, whose elements are the coordinates of each voxel in the local neighborhood and c_0 through c_9 are the coefficients of the 2nd-order polynomial. The value of $\mathbf{d}_{est}$ at a given point **p** can be expressed as

$$\mathbf{d}_{est} = \frac{1}{2}\mathbf{p}^T H \mathbf{p} + \mathbf{p}^T \mathbf{g} + c_0, \qquad (2)$$

where the gradient of the polynomial **g** and the Hessian matrix *H* are computed as

$$\mathbf{g} = \begin{vmatrix} c_1 \\ c_2 \\ c_3 \end{vmatrix} \quad \mathrm{H} = 2 \begin{vmatrix} c_4 & c_7 & c_8 \\ c_7 & c_5 & c_9 \\ c_8 & c_9 & c_6 \end{vmatrix}. \tag{3}$$

Singular value decomposition can calculate the eigenvectors and eigenvalues of *H*, which define the three eigenvectors of the polynomial and the second derivative values along each eigenvector. The center of the polynomial is calculated to be

$$\mathbf{p}_{center} = -H^{-1}\mathbf{g}. \tag{4}$$

Given the first eigenvector $\mathbf{v}_1$, the point along the first eigenvector of the polynomial that is closest to the center of the neighborhood can be calculated to be

$$\mathbf{p}_{closest} = \mathbf{v}_1\mathbf{v}_1^T\mathbf{p}_{center}. \tag{5}$$

4.3 Surface finding

Figure 10(a) illustrates how a second-order 3D polynomial approximates the local density of detected points near a voxel. These polynomials can be aggregated together to approximate a larger and more complex surface, as illustrated in Figure 10(b). Each polynomial has three eigenvectors and the first two are parallel to the local surface. A sequence of neighboring polynomials imply a surface, and the first two eigenvectors of each polynomial are tangential to that surface.

A set of discrete L2 points can represent this surface by sampling each location on the surface that is closest to any given voxel. The white square in Figure 10(a) is $\mathbf{p}_{\text{center}}$ as described by Equation 4, the point of absolute maximum in the direction of every eigenvector and every point along the first eigenvector is a point of maximum density in the direction of the second eigenvector. The white circle in Figure 10(a) represents $\mathbf{p}_{\text{closest}}$ as defined by Equation 5, the point along the first eigenvector that is closest to the center of the neighborhood in the lower-right voxel. The algorithm algebraically calculates the coordinates of the polynomial center, the closest point along the first eigenvector, and the closest point along the plane defined by the first and second eigenvectors. The intensity of each

point is set equal to the value of the polynomial at those locations, and those values are compared to a threshold value. Locations of relative maximum values are saved as L2 points if they meet the threshold value.

Figure 10(b) illustrates the detection density raster as it would be approximated by 2nd-order polynomials. The white dots are the L2 points that trace out the reflective surfaces.

Figure 9. A cross-section of the raster showing (a) the number of detected photons within each voxel and (b) the result of smoothing with the least-squares filter.

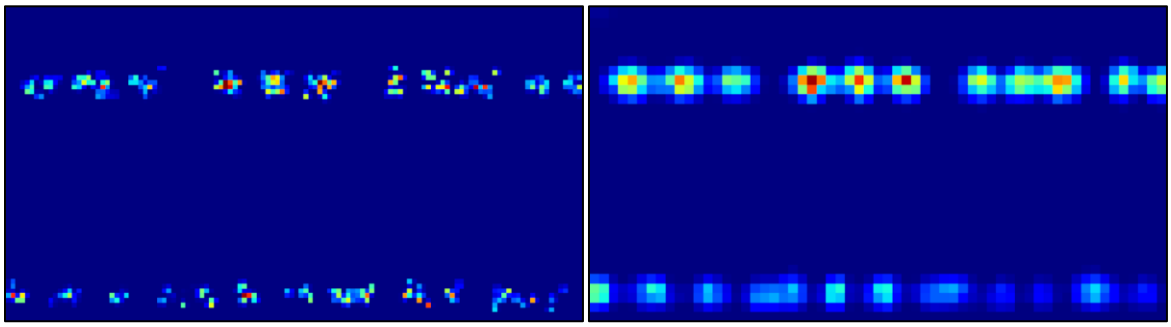

a b

Figure 10. (a) The filtered raster approximates a local region relative to the bottom right voxel. (b) L2 points are spaced along contour lines of maximum density, which trace out surfaces.

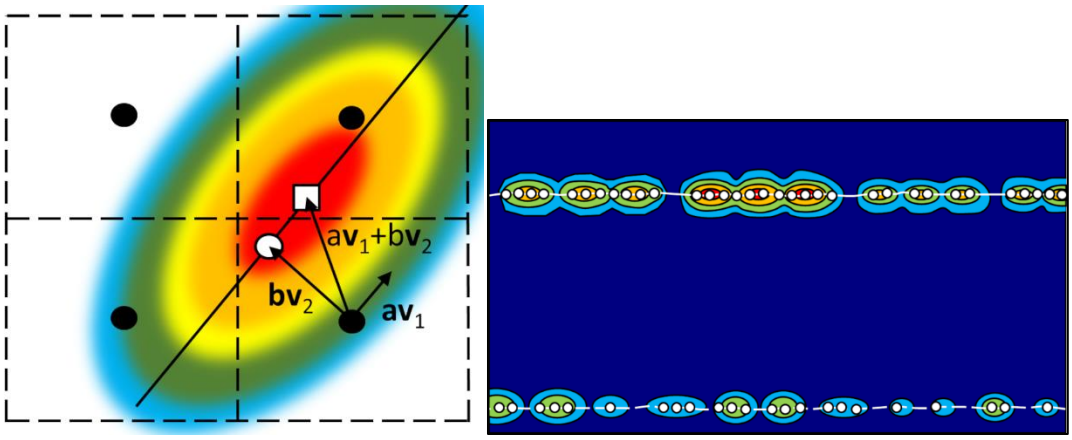

a b

5 Discussion

Inspection of the Bridge Sign output of both the artificial scene and the terrestrial lidar scene shows that the L2 point cloud outputs match the original scene with good fidelity and image interpretability. There are no spurious points above the ground, showing that the effects of background light and dark current have been removed. Furthermore, there is no apparent patterning on the ground surface due to the uneven scan pattern of the sensor.

Figure 3(d,e) illustrates how the algorithm handles the unavoidable tradeoff between feature sensitivity and surface integrity. For low SNR imagery, it may not be possible to distinguish between actual gaps in a surface and patches of lower-than-normal returns due to signal variance. The spoke target imagery shows a reasonable tradeoff between distinguishing the wheel spokes and filling in gaps in the surface. The spoke edges do have a ragged quality, which is reasonable given the L1 SNR shown in Figure 3(d), but they also correctly maintain a flat and level surface, with no curling up or down and no melted-surface type of distortion. The height values of the spoke target surface in the L1 point cloud have a standard deviation of 5.2 cm and the height values of the target in the filtered L2 point cloud have a standard deviation of 4.2 cm.

Figure 4(c) shows how much sharpness was lost by coincidence processing. The 15 cm bars are merged into a single rectangle, although the next largest set of 17.5 cm bars are still clearly distinguishable. This corresponds to approximately two times the IFOV of 9 cm.

Figure 5(c) shows that Bridge Sign preserves the shape of the round upper surface of the coil target without any flattening-type of effect, although lower surfaces are lost due to lidar shadow. Analysis of the terrestrial lidar scene shows that tree foliage is represented by rounded surfaces in the L2 data, although it is represented by 3D clouds of points in the L1 data. Nevertheless, the foliage does not show any flattening-type effect that would represent the foliage as flat horizontal planes, which would cause them to be confused with man-made features.

6 Conclusion

The use of synthetic imagery allows us to control the main sensor parameters that affect image quality and compare output quality with the original scene. This comparison demonstrates that the Bridge Sign algorithm produces output imagery with good fidelity and interpretability. All else being the same, generating higher quality L2 point clouds can enable better quality image products, such as digital surface models for topographic mapping or more accurate feature classification. Alternatively, improved coincidence processing can enable satisfactory image quality at lower laser transmitter powers than would otherwise be required. Future work may improve image quality by using a different windowing filter. For instance, the signal-to-noise ratio of the imagery varies across the scene, so a filter that dynamically adjusts for that could produce better results. It would also be valuable to develop new techniques for coincidence processing that are more computationally efficient since Bridge Sign and other current coincidence processing require more computing resources than can be easily integrated into a sensor package.

References

Albota, M. A., R. M. Heinrichs, D. G. Kocher, D. G. Fouche, B. E. Player, M. E. O'Brien, B. F. Aull, J. J. Zayhowski, J. Mooney, B. C. Willard, and R. R. Carlson. 2002. "Three-dimensional imaging laser radar with a photon-counting avalanche photodiode array and microchip laser." *Applied Optics* **41**(36) 7671-7678.

Amenta, N., and M. Bern. 1999. "Surface reconstruction by Voronoi Filtering." *Discrete and Computational Geometry* **22** 481-504.

Bressel, C., I. Itzkan, J. E. Nunes, and F. Hoge. 1977. "Airborne oceanographic lidar system." *Proc. 11th Int. Symp. Rem. Sens. Env.* **2** 1259-1268.

Clifton, W. E., B. Steele, G. Nelson, A. Truscott, M. Itzler, and M. Entwistle. 2015. "Medium altitude airborne Geiger-mode mapping LIDAR system." *Proc. SPIE 9465*.

Degnan, J., R. Machan, E. Leventhal, D. Lawrence, G. Jodor, and C. Field. 2008. "Inflight performance of a second-generation photon-counting 3D imaging lidar." *Proc. SPIE 6950*.

Dumanis, D. 2016. "Airborne optical systems test bed (AOSTB)" Technical Report, MIT Lincoln Laboratory, https://apps.dtic.mil/dtic/tr/fulltext/u2/1033486.pdf

Eldar, Y., M. Lindenbaum, M. Porat, and Y. Y. Zeevi. 1997. "The farthest point strategy for progressive image sampling." *IEEE Trans. on Image Proc.* **6**(9) 1305-1315.

Gonzalez, R. C., and R. E. Woods. 2008. *Digital Image Processing*. Upper Saddle River, New Jersey: Pearson Prentice Hall.

Gray, G. 2011. "High Altitude Lidar Operations Experiment (HALOE) – Part 1, System Design and Operation." *Proc. Of Military Sensing Symposium, Active Electro-Optic Systems*.

Itzler, M., M. Entwistle, M. Owens, K. Patel, X. Jiang, K. Slomkowski, S. Rangwala, P. F. Zalud, T. Senko, J. Tower, and J. Ferraro. 2010. "Geiger-mode avalanche photodiode focal plane arrays for three-dimensional imaging LADAR." *Proc. of SPIE 7808*.

Knowlton, R. 2011. "Airborne ladar imaging research testbed." *MIT Lincoln Lab. Tech Notes*.

Kondratko, P., R. Irwin, A. Strevey, J. Medbery, and P. Earhart. 2019. "Geiger-mode avalanche photodetector camera technology at Ball Aerospace." *Proc. SPIE 11005*.

Marino, R. M., and W. R. Davis. 2005. "Jigsaw: a foliage-penetrating 3D imaging laser radar system." *Lincoln Laboratory Journal* **15**(1), 23-36.

Stevens, J. R., N. A. Lopez, and R. R. Burton. 2011. "Quantitative data quality metrics for 3D laser radar systems." *Proc. of SPIE 8037*.

Stoker, J. M., Q. Abdullah, A. Nayegandhi, and J. Winehouse. 2016. "Evaluation of single photon and Geiger mode lidar for the 3D elevation program." *Remote Sensing* **8**, 767.

Vasile, A. N., L. J. Skelly, M. E. O'Brien, D. G. Fouche, R. M. Marino, R. Knowlton, M. J. Khan, and R. M. Heinrichs. 2012. "Advanced coincidence processing of 3D laser radar data." *Adv. Vis. Comp.: 8th Int. Symp.* 382-393.

Acronyms

APD	avalanche photo-diodes
ALIRT	Airborne Ladar Imaging Research Testbed
FPA	focal plane array
GmAPD	Geiger-mode avalanche photo-diode
GPS	global positioning unit
HALOE	High-Altitude LIDAR Operations Experiment
IFOV	instantaneous field-of-view
IMU	inertial measurement unit
MAPCP	Maximum A Posteriori Coincidence Processing
MIT	Massachusetts Institute of Technology
MPSCP	Multiple-Peak Spatial Coincidence Processing

REPORT DOCUMENTATION PAGE

Form Approved
OMB No. 0704-0188

1. REPORT DATE *(DD-MM-YYYY)*	2. REPORT TYPE	3. DATES COVERED *(From - To)*
February 2020	Final	

4. TITLE AND SUBTITLE

Coincidence Processing of Photon-Sensitive Mapping Lidar Data

5a. CONTRACT NUMBER

5b. GRANT NUMBER

5c. PROGRAM ELEMENT NUMBER
62784

6. AUTHOR(S)

Christian Marchant, Ryan Kirkpatrick, and David Ober

5d. PROJECT NUMBER
855

5e. TASK NUMBER
23

5f. WORK UNIT NUMBER

7. PERFORMING ORGANIZATION NAME(S) AND ADDRESS(ES)

Geospatial Research Laboratory
U.S. Army Engineer Research and Development Center
7701 Telegraph Road
Alexandria, VA 22315

8. PERFORMING ORGANIZATION REPORT NUMBER

ERDC/GRL TR-20-1

9. SPONSORING / MONITORING AGENCY NAME(S) AND ADDRESS(ES)

U.S. Army Corps of Engineers
Washington, DC 20314-1000

10. SPONSOR/MONITOR'S ACRONYM(S)

11. SPONSOR/MONITOR'S REPORT NUMBER(S)

12. DISTRIBUTION / AVAILABILITY STATEMENT

Approved for public release; distribution is unlimited.

13. SUPPLEMENTARY NOTES

14. ABSTRACT

Photon-sensitive mapping lidar systems are able to image at greater collection area rates and ranges than linear-mode systems. However, these systems also experience greater noise levels due to shot noise, image blur, and dark current, which must be filtered out before the imagery can be exploited. Described in this report is a synthetic test data set of imagery from a notional airborne Geiger-mode lidar. Also described is the Bridge Sign algorithm, which uses a least-squares technique for noise filtering. The algorithm's performance was validated using synthetic test imagery of both a toy scene and of a realistic scene, which were generated using the parameters of a notional airborne Geiger-mode system. Analysis of the results shows the technique effectively removes noise and preserves fine details with good fidelity.

15. SUBJECT TERMS

Optics, Algorithms, Light, Electronic data processing, Mapping, Lasers, Topography, Photonics, Photon detectors, Lidar, Optical radar

16. SECURITY CLASSIFICATION OF:			17. LIMITATION OF ABSTRACT	18. NUMBER OF PAGES	19a. NAME OF RESPONSIBLE PERSON
a. REPORT	b. ABSTRACT	c. THIS PAGE			19b. TELEPHONE NUMBER *(include area code)*
Unclassified	Unclassified	Unclassified	SAR	30	